Dynamics of the DNA Binding Domain of the Fructose Repressor from the Analysis of Linear Correlations between the $^{15}N-^{1}H$ Bond Spectral Densities Obtained by Nuclear Magnetic Resonance Spectroscopy

Carine van Heijenoort,[‡] François Penin,[§] and Eric Guittet*[,‡]

Institut de Chimie des Substances Naturelles, Laboratoire de Résonance Magnétique Nucléaire, 1 Avenue de la Terrasse, Centre National de la Recherche Scientifique, F-91190 Gif sur Yvette, France, and Institut de Biologie et Chimie des Protéines, Unité Propre de Recherche 412 du Centre National de la Recherche Scientifique, 7 Passage du Vercors, F-69367 Lyon, France

Received July 14, 1997; Revised Manuscript Received October 15, 1997

ABSTRACT: The spectral densities of the backbone and arginine side chain NH bonds of the DNA binding domain of the fructose repressor (FruR) were extensively analyzed in order to extract reliable motions parameters. An accurate measurement of ^{15}N NMR relaxation rates allowed their calculation at three frequencies, zero, ω_N, and $\omega_H + \omega_N$, using a reduced matrix approach. Linear correlations were found between $J(\omega_N)$ and $J(0)$ and between $\langle J(\omega_H)\rangle$ and $J(0)$. The analysis of the compatibility between the motions parameters obtained independently from the two correlation lines allowed further development of the linear correlation approach proposed recently [Lefèvre, J. F., Dayie, K. T., Peng, J. W., and Wagner, G. (1996) *Biochemistry 35*, 2674−2686]. The results demonstrate (i) the existence of a concerted motion along the whole backbone with a global correlation time equal to 5.95 ns·rad^{-1}, and (ii) the presence of complex internal movements at an intermediate time scale around 1 ns. The extracted motion parameters have been related to those obtained with the extended Lipari and Szabo approach but are incompatible with those obtained using the usual simple Lipari and Szabo approach. They were correlated to the features of the NMR structure of FruR(1−57)*. Some residues in the turns and in the third helix experience slow motions in the micro- to millisecond time scale. Side-chain motions are not correlated to the backbone dynamics. A direct examination of spectral densities reveals a higher flexibility for the side chains of arginines that are not involved in ionic bridges.

Relaxation rates of the $\{^{1}H^{N},^{15}N\}$ spin systems are related to the motion of the $^{1}H^{N}-^{15}N$ bond through their spectral densities at the following five frequencies: 0, ω_N, $\omega_H + \omega_N$, ω_H and $\omega_H - \omega_N$ (*1*, *2*). The five spectral densities give the proportion of the energy of the dipole−dipole and CSA[1] interactions used for the motions at the corresponding frequencies. They represent the highest level of information that can be obtained about motions from the measurements of relaxation rate constants. Therefore, the first goal should be to extract them from the experimental data. However, since the direct calculation of the five spectral densities from NMR data leads to untrustworthy results (*3*, *4*), we used the more reliable reduced matrix approach (*4*−*7*) to evaluate the three spectral densities $J(0)$, $J(\omega_N)$, and $J(\omega_H + \omega_N)$, and the proton−proton relaxation term ρ_{HH} from the four relaxation NMR constants, $R_N(N_z)$, $R_N(N_{x,y})$, $R_{HN}(2H_zN_z)$, and heteronuclear ($^{1}H \rightarrow {}^{15}N$) nOes. A first straightforward analysis of these spectral densities is already very informative. It provides an image of the distribution of motions at different time scales along the protein backbone, from the picosecond to the millisecond range. To extract more pictorial information about the dynamics of the macromolecule, accuracy has to be put apart since the use of models for motions based on more or less simple assumptions has to be done. The Lipari and Szabo "model-free" approach (*8*, *9*) is today the most widely used model for the analysis of the ^{15}N relaxation NMR data. It has the advantage of being simple and is possibly one of the most suitable for the analysis of the only three experimental data usually measured: $R_N(N_z)$, $R_N(N_{x,y})$, and heteronuclear ($^{1}H \rightarrow {}^{15}N$) nOes. However, it cannot take into account the diversity of internal motion time scales. Its physical relevance is thus limited to fully structured macromolecules for which internal motions are very fast and highly restricted. Moreover, to correctly reproduce experimental data, it is usually necessary to consider an extra so-called "exchange contribution" term whose physical meaning is vague. To take into account the deviation from the simple model-free approach, an extended form of the model has been developed using two time scales for the internal motions (*10*, *11*). However, this extended model has the disadvantage of introducing a supplementary parameter without additional experimental data. The physical relevance of the results of the fits can then become questionable. Recently, from the analysis of relaxation data

* To whom correspondence should be addressed: E-mail guittet@icsn.cnrs-gif.fr; Fax 33-1-69077247.

[‡] Institut de Chimie des Substances Naturelles.

[§] Institut de Biologie et Chimie des Protéines.

[1] Abbreviations: 2D, two-dimensional; 3D, three-dimensional; CPMG, Carr−Purcell−Meiboom−Gill; CSA, chemical shift anisotropy; DBD, DNA binding domain; DD, dipole−dipole; FID, free induction decay; FruR(1−57)*, 57 N-terminal residues of FruR in fusion with a LQHHHHHH C-terminal sequence extension; GARP, globally optimized alternating phase rectangular pulse; GIFA, general fixed point algorithm; HSQC, heteronuclear single quantum correlation spectroscopy; nOe, nuclear Overhauser effect; rms, root-mean-square.

S0006-2960(97)01706-6 CCC: $15.00
Published on Web 03/26/1998

obtained on a series of proteins and from theoretical considerations on the shape of the spectral density functions of proteins, Lefèvre et al. (*7*) showed that a linear correlation usually exits between $J(0)$ on one hand and $J(\omega_N)$ and $J(\omega_H)$ on the other hand for most of the backbone NH bonds. They analyzed more specifically the linear correlation between $J(\omega_N)$ and $J(0)$ on the backbone NH bonds of the DNA binding domain of GAL4. They showed that this experimental correlation allows the extraction of dynamic information about the distribution of global and internal motions along proteins backbone by using only a minimal number of assumptions on the nature of motions. They proposed that the existence of such a linear correlation is due to collective motions of NH vectors along the backbone of proteins at a limited number of time scales. We propose here to thoroughly study this correlation approach and to extend this analysis to the NH bonds of arginine side chains. The compatibility of the motion parameters obtained from a linear correlation between $J(0)$ and $J(\omega_N)$ on one hand and between $J(0)$ and $J(\omega_H)$ on the other hand was examined in order to ascertain their relevance. Since most of the issues made on proteins dynamics are today drawn from Lipari and Szabo analysis of relaxation parameters, we also investigated the simple and extended Lipari and Szabo approaches in order to confront the results of the three approaches. The results on dynamics thus obtained were then related to the structural characteristics of the FruR DBD.

The fructose repressor protein, FruR, belongs to the LacI family of bacterial DNA-binding proteins that bind DNA via a highly conserved N-terminal helix−turn−helix motif (*12*). It has been shown that its isolated DNA binding domain FruR(1−57)* retains a high specificity and binding affinity for its DNA operator (*13*). The 3D structure of the FruR DBD has been obtained from ^{1}H and ^{15}N NMR data (*14*) and is shown in Figure 1. The helix−turn−helix motif, stabilized by a third helix, constitutes a well-defined core from residues 2 to 45. The connecting segment between helices II and III is highly structured and stabilized by a hydrogen-bond network extending from residues 24 to 31 and by the aromatic ring stacking of tyrosines 19 and 28. It has been proposed that residues protruding at the surface in this region are likely to be involved in DNA binding and recognition specificity (*14*). Especially, comparison with the known structures of LacI and PurR bound to their operators (*15, 16*) suggests that the side chains of tyrosine 28 and arginine 29 are good candidates for direct contact with the major groove of DNA upon binding. The 3D structures of the purine repressor dimer, PurR, bound to to its DNA operator (*15*) and of the *lac* repressor DBD dimer bound to a 22 base pair DNA operator (*16, 17*) highlighted the formation of a fourth so-called "hinge" helix upon binding in the DNA minor groove. In contrast, the hinge helix is unfolded in free PurR and LacI DBD as also observed for free FruR DBD (Figure 1).The coil to hinge helix transition results not only from specific DNA binding but also requires protein−protein interaction between the two related helices (*17*). To better understand the contribution of the motions involved in the interaction of these proteins with their DNA operators, we have undertaken the analysis of the dynamics of FruR DBD. We report here the dynamic analysis of FruR-(1−57)* free in solution.

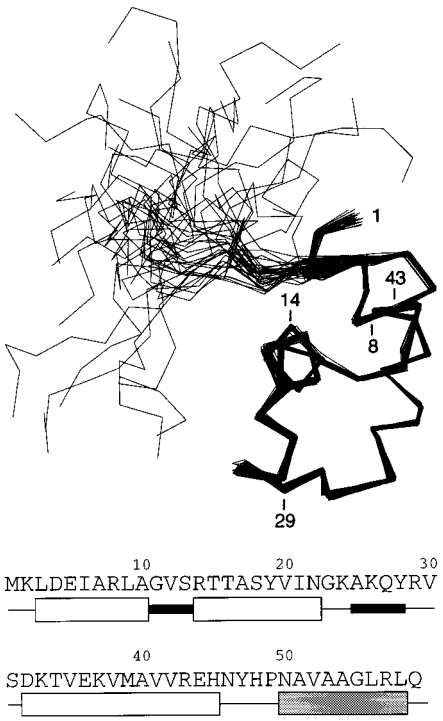

FIGURE 1: Sequence, secondary structure, and superimposition of the 34 final calculated conformers of FruR(1−57)*, showing the well-structured N-terminal subdomain and the flexibility of the C-terminal region (*7*). White and black boxes indicate α-helix and turn, respectively. Grey box indicates the putative helix IV, which is unfolded in the absence of complexation with DNA operator. The reader is looking down helix II (residues 14−22) on the left, helix III (residues 32−45) is nearly vertical, and helix I (residues 3−10) is tilted by about 45°. The α-carbon chains on the 34 conformers were superimposed from residues 1 to 47 using ANTHEPROT software tools (*29*). Arginine residues are labeled as indicated. For clarity, R57 is not indicated.

MATERIALS AND METHODS

NMR Sample. FruR DBD [FruR(1−57)*] was cloned, overproduced as a uniformly ^{15}N labeled sample, and purified as previously described (*13, 14*). All experiments were performed at 20 °C on a 2 mM ^{15}N-labeled protein sample in solution in a 20 mM phosphate buffer (pH = 5.9) containing 0.1 M NaCl, 70 mM NH_4Cl, 5% D_2O, and 0.05% sodium azide. NMR spectra were acquired on a Bruker AMX-600 spectrometer equipped with a 5 mm triple-resonance gradient probe with an actively shielded *z* gradient.

Sequences and Parameters for the Evaluation of Relaxation Rate Constants. The pulse sequences used to determine ^{15}N $R_1(N_z)$, $R_2(N_{xy})$, and $R_z(H_zN_z)$ values were similar to those described (*2, 18*). To minimize artifacts, gradients were inserted during the intervals when the spin system is in the H_zN_z state, for which H_z and N_z denote the *z* components of the $^1H^N$ and ^{15}N magnetizations, respectively. A recycle delay of 4 s was employed and ^{15}N decoupling during acquisition was performed using a GARP sequence (*19*). $R_1(N_z)$ experiments were performed with 10 relaxation delays *T*: 0.02, 0.05, 0.075, 0.150, 0.250, 0.4, 0.7, 1, 3, and 5 s. For $R_2(N_{xy})$ experiments, a CPMG pulse train with 900 μs between pulses was used during the relaxation delay as previously described (*18*). The ^{15}N pulse duration was 42 μs. Ten experiments were acquired, with relaxation delays *T* of 0.01, 0.02, 0.05, 0.1, 0.2, 0.4, 0.8, 1.2, 2, and 3 s. The delay between the 180° proton pulses used to suppress the

DD−CSA cross-relaxation effects was 2.5 and 3.92 ms for the $R_1(N_z)$ and $R_2(N_{xy})$ experiments, respectively. $R_z(H_zN_z)$ were obtained from 10 experiments with relaxation delays T of 5, 10, 25, 50, 80, 130, 200, 300, 500, and 750 ms. In the three sets of experiments, the points corresponding to different relaxation delays were acquired in an interleaved manner to avoid any bias that could arise from the progressive shim degradation.

For heteronuclear $^1H-^{15}N$ nOes, special care was taken to avoid large errors that can occur when dealing with protons in fast exchange with the solvent. To achieve that goal, a carefully optimized water flip-back pulse (*20*) was added before the last proton 90° pulse in the experiment without saturation. A relaxation delay equal to 4 s between each scan was sufficient to obtain a complete relaxation of water magnetization and to avoid any exchange effect. Moreover, the two experiments with and without proton saturation were acquired in an interleaved manner, FID by FID. A relaxation delay of 10 s was used before the FIDs of the experiment without saturation. Carrier frequencies were set at 107 ppm in the $F1$ dimension (^{15}N) and 7.3 ppm in the $F2$ dimension (at the center of the $^1H^N$ resonances). Spectral widths were 67 ppm in the $F1$ (^{15}N) dimension and 6.7 ppm in the $F2$ ($^1H^N$) dimension. A Watergate off-resonance sequence was used just prior to acquisition to suppress the solvent resonance (*21*). Each 2D data set consisted of 1024 complex data points in t_2 and 128 complex points in t_1.

Data Processing and Analysis. NMR spectra were processed using the GIFA software (*22*). A pure cosine bell and a matched 6 Hz exponential filter were applied along t_1 and t_2, respectively. The data were zero-filled twice along t_1 and once along t_2 prior to Fourier transform. Finally, a baseline correction was applied in both dimensions using the corresponding GIFA automatic baseline routine. Cross-peak intensities were determined from peak heights using the GIFA peak-picking routine (*23*). The relaxation rate constants $R_N(N_z)$, $R_N(N_{x,y})$, and $R_{HN}(2H_zN_z)$ were obtained from nonlinear fits to monoexponential functions using the Levenburg−Marquardt algorithm (*24*). Analytical calculation of derivatives were used. The uncertainties, due to random errors in the measured heights, were determined from 500 Monte Carlo simulations. The width of the Gaussian distribution of height errors was set to 5 times the rms base plane noise level (*23*). It was in good agreement with the standard deviation in the peak heights obtained by comparing the results from two duplicate spectra acquired for each set of measurements. nOe enhancements were obtained as the ratio of the peak heights in the spectra recorded with and without saturation of protons during the relaxation delay. The uncertainties of these nOes were the sum of the uncertainties in the peak intensities of each experiment. The rate $R_N(H_z^N \leftrightarrow N_z)$ for cross relaxation between the amide proton and nitrogen was then calculated according to

$$\mathrm{nOe} = 1 + \frac{\gamma_H}{\gamma_N}\frac{R_N(H_z^N \leftrightarrow N_z)}{R_N(N_z)} \qquad (1)$$

Spectral Density Mapping Using the Reduced Matrix Approach. The three spectral densities $J(0)$, $J(\omega_N)$, and $\langle J(\omega_H)\rangle$ were calculated from the three most reliably measured relaxation rate constants $R_N(N_z)$, $R_N(N_{x,y})$, and $R_N(H_z^N \leftrightarrow N_z)$, using the reduced matrix $\mathbf{M}_{red,3}$ (*4*−*7*):

$$J_{red,3} = \mathbf{M}_{red,3} \times R_{red,3} \qquad (2)$$

that is, explicitly,

$$\begin{bmatrix} J(0) \\ J(\omega_N) \\ \langle J(\omega_H)\rangle \end{bmatrix} = \begin{bmatrix} \frac{-3}{4(3d+c)} & \frac{3}{2(3d+c)} & \frac{-9}{10(3d+c)} \\ \frac{1}{(3d+c)} & 0 & \frac{-7}{5(3d+c)} \\ 0 & 0 & \frac{1}{5d} \end{bmatrix} \times \begin{bmatrix} R_N(N_z) \\ R_N(N_{x,y}) \\ R_N(H_z^N \rightarrow N_z) \end{bmatrix} \qquad (3)$$

where d is the weight of the dipolar interactions between the amide nitrogen and proton and c is the strength of the chemical shift anisotropy. The constants are given by

$$d = \left(\frac{\mu_0}{4\pi}\right)^2 \frac{\hbar^2 \gamma_H^2 \gamma_N^2}{4 r_{HNN}^6} \qquad c = \frac{\omega_N^2 \delta_{CSA}^2}{3} \qquad (4)$$

where μ_0 is the permeability of vacuum, $\hbar$ is the Planck's constant divided by 2π, and γ is the gyromagnetic ratio ($\gamma_H = 2.6752 \times 10^8$ rad·s^{-1}·T^{-1} and $\gamma_N = -2.711 \times 10^7$ rad·s^{-1}·T^{-1}). For a magnetic field of 14.1 T, an internuclear distance $^{15}N-^1H$ r_{H^NN} of 0.102 nm, and a chemical shift anisotropy δ_{CSA} of −160 ppm, $d = 1.2986 \times 10^9$ rad^2·s^{-2} and $c = 1.246 \times 10^9$ rad^2·s^{-2}.

The additional measurement of $R_{HN}(2H_zN_z)$ allows the evaluation of the longitudinal cross-relaxation rate of amide proton to other neighboring protons $\rho_{H^NH^i}$ via (*7*)

$$\rho_{H^NH^i} = -R_N(N_z) + \frac{4}{5}R_N(H_z^N \rightarrow N_z) + R_{HN}(2H_zN_z) \qquad (5)$$

This approach leads to a value for $\langle J(\omega_H)\rangle$ very close to the true value of $J(\omega_N + \omega_H)$. Indeed, $\langle J(\omega_H)\rangle$ is directly obtained from the $^1H-^{15}N$ cross-relaxation rate constant, whose dominant contribution is $J(\omega_N + \omega_H)$. The value for $\langle J(\omega_H)\rangle$ also corresponds to the $J(\omega_N + \omega_H)$ of Ishima and Nagayama (*25*) and the $J(0.87\omega_H)$ of Farrow et al. (*26*).

Random Gaussian noise was added to the relaxation rate constants for the evaluation of the uncertainties. The width of the Gaussian distribution around each relaxation rate constant was set to the uncertainty obtained as described above. One hundred values were extracted independently for each relaxation rate constant, leading to a set of 100 quartets ($J(0)$, $J(\omega_N)$, $\langle J(\omega_H)\rangle$, $\rho_{H^NH^i}$) for each NH bond. The results retained were the mean values, with uncertainties equal to the standard deviations of the distributions obtained.

Spectral Density Analysis. The three spectral densities $J(0)$, $J(\omega_N)$, and $\langle J(\omega_H)\rangle$ represent the proportion of the total energy used for motions at each corresponding frequency. A comparative analysis of the spectral densities along the sequence thus gives a straightforward idea of the different distribution of the frequencies of NH bond motions along the backbone and in the arginine side chains. Lefèvre et al. (*7*) analyzed several relaxation data obtained on various proteins and found often the existence of a linear correlation

between $J(0)$ and $J(\omega_N)$ and between $J(0)$ and $\langle J(\omega_H)\rangle$:

$$J(\omega_N) = \alpha_N J(0) + \beta_N \quad (6)$$

$$\langle J(\omega_H)\rangle = \alpha_H J(0) + \beta_H \quad (7)$$

To go further into the interpretation of this observed correlation, a minimal number of assumptions have to be made on the shape of the spectral density function, and thus on the different motions of the NH bonds in proteins. The first usual assumption is that the global reorientation of the whole protein in the nanosecond range is not correlated with the internal motions. These motions can themselves consist of several uncorrelated motions (*27*). The spectral density function is then decomposed as a weighted sum of independent contributions $J_k(\omega)$ in which the first component ($k = 0$) corresponds to the overall motion:

$$J(\omega) = a_0 J_0(\omega) + \sum_{k=1}^{M} a_k J_k(\omega) \quad (8)$$

a_k is the scaling factor of the spectral density function $J_k(\omega)$ characterizing each independent motion and $\sum_k a_k = 1$.

Spectral Density Function Models. (A) Isotropic Brownian Motions. For the analysis of the correlation between the three experimental spectral densities, we just made the additional assumption that the global reorientation of the protein is dominated by an isotropic brownian motion with a unique global correlation time τ_c. This hypothesis seems reasonable in the case of the monodomain FruR DBD. The corresponding correlation function is then a simple decaying exponential (*1*):

$$G(\tau) = \frac{1}{5}\exp\left(-\frac{t}{\tau_c}\right) \quad (9)$$

The corresponding spectral density function is

$$J(\omega) = \frac{2}{5}\frac{\tau_c}{1+\omega^2\tau_c^2} \quad (10)$$

All the data extracted from this analysis have been evaluated from the set of a hundred values of [$J(0)$, $J(\omega_N)$, $\langle J(\omega_H)\rangle$] obtained as already described. As previously, the mean values were retained, with an uncertainty equal to the standard deviation of the resultant distribution.

Then, we considered the two most currently used models.

(B) Lipari and Szabo Analysis. In this approach, an additional assumption is made on the shape of the correlation function, and thus of the spectral density function. The initial fast decay of the correlation function, connected with fast internal motions, is approximated by a decaying monoexponential function. Fast internal motions are characterized by the square of a generalized order parameter S^2 and an internal correlation time τ_e, sometimes called "effective correlation time" for the internal motions. The expression for the spectral density function is (*8, 9*)

$$J(\omega) = \frac{2}{5}\frac{S^2\tau_c}{1+\omega^2\tau_c^2} + \frac{2}{5}\frac{(1-S^2)\tau_i}{1+\omega^2\tau_i^2} \quad \text{with}$$

$$\tau_i^{-1} = \tau_c^{-1} + \tau_e^{-1} \quad (11)$$

τ_c is the global rotational correlation time of the protein. A set of 100 triplets (τ_c, S^2, τ_e) was obtained for each NH vector of the backbone and arginine side chain by a least-squares fit of eq 11 to the experimental set [($J(0)$, $J(\omega_N)$, $\langle J(\omega_H)\rangle$]. A Levenburg−Marquardt minimization procedure was used. The disparity of τ_c along the sequence is usually rationalized by the existence of slow exchange processes, in the micro- to millisecond time scale. These processes are responsible for line broadening. They contribute to an adiabatic relaxation pathway leading to an increase of $R_N(N_{x,y})$ which is entirely transferred to the value of $J(0)$. By use of eq 3, the value of $J(0)$ can then be decomposed as the sum of an exchange term $J_{ex}(0)$ and a "Lipari and Szabo" term $J_{LS}(0)$:

$$J(0) = J_{ex}(0) + J_{LS}(0) \quad (12a)$$

$$J_{ex}(0) = \frac{3}{2(3d+c)}R_{ex}^N \quad (12b)$$

$$J_{LS}(0) = \frac{2}{5}S^2\tau_c + \frac{2}{5}(1-S^2)\tau_i \quad (12c)$$

Since the model assumes a unique global correlation time for the overall rotational reorientation of the protein, a series of minimizations was performed using a given τ_c for all the NH vectors. Seven different values of τ_c (3, 3.2, 3.5, 4, 4.5, 5, and 5.5 ns·rad^{-1}) were tested. Sets of triplets [$J_{ex}(0)$, S^2, τ_e] were obtained for each NH vector of the backbone and arginine side chains using the procedure described above.

(C) Extended Lipari and Szabo Model (10, 11). Internal motions are here supposed to take place on two distinct time scales. The spectral density function is then split into three terms.

$$J(\omega) = \frac{2}{5}\frac{S^2\tau_c}{1+\omega^2\tau_c^2} + \frac{2}{5}\frac{S_f^2(1-S_s^2)\tau_s'}{1+(\omega\tau_s')^2} + \frac{2}{5}\frac{(1-S_f^2)\tau_f'}{1+(\omega\tau_f')^2} \quad (13a)$$

The effective correlation times for the slower, τ_s, and faster, τ_f, time scale internal motions are obtained from the relations $(\tau_s') = \tau_c^{-1} + \tau_s^{-1}$ and $(\tau_f') = \tau_c^{-1} + \tau_f^{-1}$, respectively. The order parameter S^2 for internal motions is the product of two order parameters, one for the slower time scale motions, S_s^2, and one for the faster time scale motions, S_f^2, with $S^2 = S_s^2 S_f^2$. To fit this model with only three experimental values, the contribution of the fastest motion to the spectral density function has to be assumed to be negligible. The spectral density function then takes the form

$$J(\omega) = \frac{2}{5}\frac{S^2\tau_c}{1+\omega^2\tau_c^2} + \frac{2}{5}\frac{(S_f^2-S^2)\tau_s'}{1+(\omega\tau_s')^2} \quad (13b)$$

Using the procedure described above, different triplets (S^2, S_f^2, τ_s) were obtained using fixed values of τ_c.

RESULTS AND DISCUSSION

Measured Rates and Reduced Spectral Densities. Figure 2A shows the three relaxation rate constants and the heteronuclear nOes at stationary state that were measured on FruR(1−57)*. The location of the secondary structures

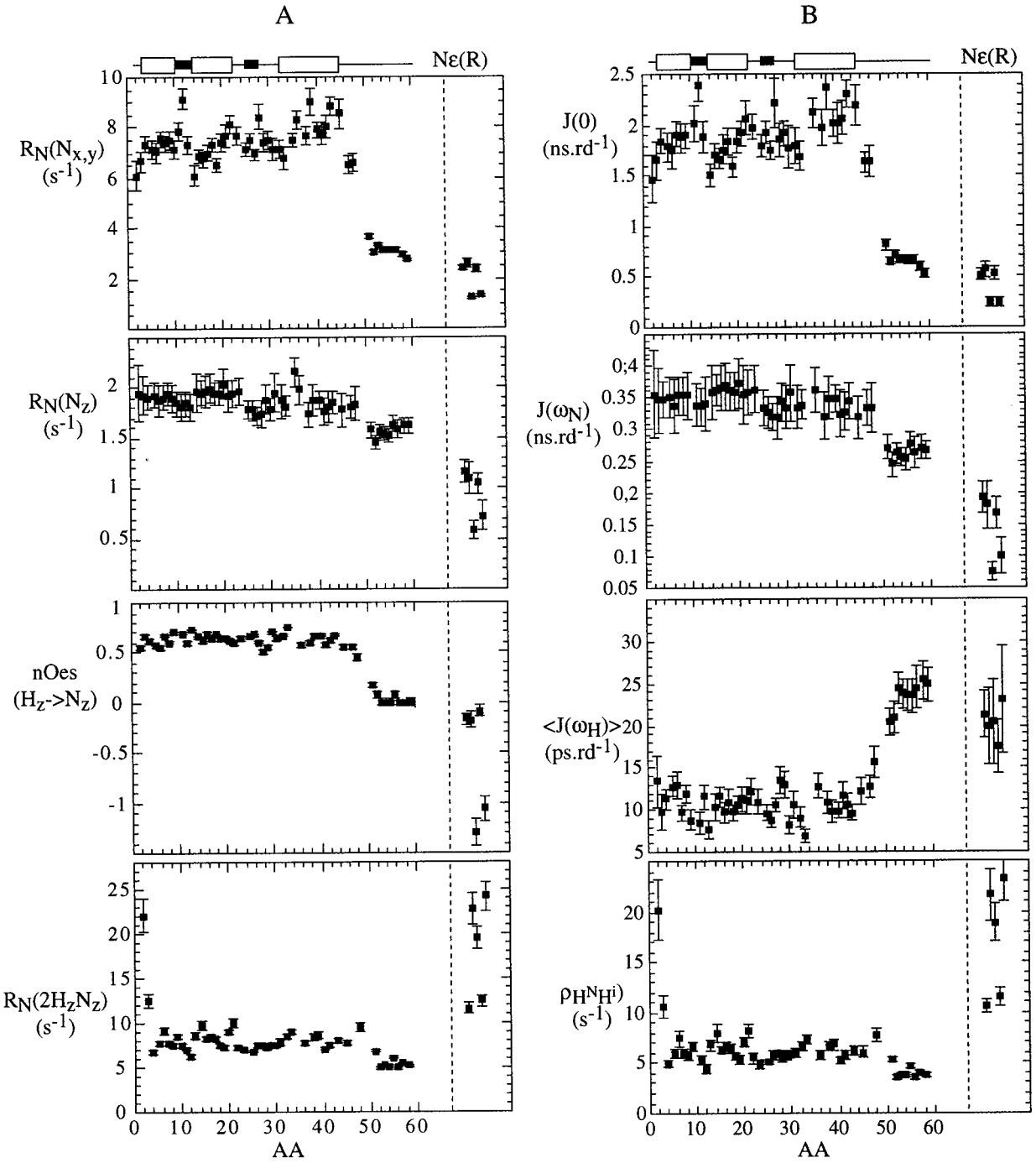

FIGURE 2: (A) Relaxation rates as a function of the primary sequence obtained for FruR(1−57)* at 20 °C. (B) Corresponding values of the three spectral densities $J(0)$, $J(\omega_N)$, and $\langle J(\omega_H)\rangle$ calculated from eq 10 and of the longitudinal cross-relaxation rate constant of amide protons to other neighboring protons, $\rho_{H^N H^i}$, calculated from eq 11. The secondary structures are represented at the top of the figure: helices are represented as white boxes and turns as black boxes. Nϵ of arginine residues are presented in the following order: R8, R14, R29, R43, and R54.

are shown on the top of the figure. The results obtained for the Nϵ of the arginine side chains are shown on the right of the figure, according to their order along the primary sequence: R8-R14-R29-R43-R57. NMR relaxation parameters were obtained on 56 out of the 69 ^{15}NHs of the protein. The N-terminal residue (Met1) and the six C-terminal histidines were not assigned. The six remaining unmeasured ^{15}NHs, K24, T34, K37, E44, N46, and N50 correspond to superposed correlation peaks in the HSQC spectra. The three reduced spectral densities $J(0)$, $J(\omega_N)$, and $\langle J(\omega_H)\rangle$ and the proton relaxation rate $\rho_{H^N H^i}$ obtained from the reduced relaxation matrix are shown in Figure 2B. The relaxation rates $R_{HN}(2H_zN_z)$ are faster than all the others and indicate a large contribution of dipolar relaxation processes between amide protons and other neighboring protons. This result legitimizes the use of the reduced matrix approach for a reliable evaluation of the spectral densities that is only based on the relaxation rate constants, that do not depend on the large proton relaxation term $\rho_{H^N H^i}$ (*7*).

The spectral densities for the NH bonds of the backbone clearly show a different behavior in the structured core (residues 3−48) and in the unfolded 50−59 segment of the protein. In the core of the protein, mean values are 1.88 ns·rad^{-1}, 0.345 ns·rad^{-1}, and 10.8 ps·rad^{-1} with standard

deviations equal to 0.22 ns·rad^{-1}, 0.015 ns·rad^{-1}, and 1.8 ps·rad^{-1}, respectively, for $J(0)$, $J(\omega_N)$, and $\langle J(\omega_H)\rangle$. In the 50−59 segment of the protein, mean values in the same order are 0.66 ns·rad^{-1}, 0.26 ns·rad^{-1}, and 23.5 ps·rad^{-1} with standard deviations equal to 0.08 ns·rad^{-1}, 0.01 ns·rad^{-1}, and 1.7 ps·rad^{-1}. NH vectors of the backbone of five residues, V12, Y28, M39, R43, and H45, show significantly higher $J(0)$ values than the mean, while $J(\omega_N)$ and $\langle J(\omega_H)\rangle$ for these residues are not smaller than the mean values. This is in favor of the hypothesis that slow movements in the micro- to millisecond range exist for these residues. These processes increase the value of the spectral density function in a very narrow frequency range, from zero to a few kilohertz, but have no influence at higher frequencies in the megahertz range. The much flatter shape of the spectral density function in the 50−59 segment indicates a dominant contribution of motions at higher frequencies than in the core. In contrast to that observed for GAL4 at 50 MHz (*7*), the values of $J(\omega_N)$ in the 50−59 segment are here significantly shorter than in the folded part. Since variations of $J(\omega_N)$ are quite small in the nanosecond range, this drop of $J(\omega_N)$ means that a large proportion of the energy is used for subnanosecond motions. From this first examination of the evolution of spectral densities along the backbone, it appears that, from a dynamic point of view, the protein can be divided in two regions (see Figure 10). The transition between the two regions is particularly abrupt and occurs between residues 48 and 50. This can be explained by a hinge role played by this small segment that connect the globular subdomain to helix IV when folded. Beyond the overall tumbling of the whole protein, this raises the problem of the reorientation of the unfolded C-terminal end relative to the globular structured core. The evaluation of a global correlation time for the whole protein using local models as in the Lipari and Szabo approach seems thus not suitable, since the correlation function of a NH bond in the nanosecond time scale will be a composite function of the reorientation of the whole protein and of each segment. The other question raised is whether these different dynamic behaviors in the two parts of the protein are due to the existence of many motions at various time scales, or to a different distribution of a limited number of motions at the same time scales. The search for correlations between $J(0)$ and $J(\omega_N)$ and between $J(0)$ and $\langle J(\omega_H)\rangle$ allowed us to answer this question (see below).

NHϵ vectors of arginine side chains also show a specific behavior (Figure 2B). $J(0)$ and $\langle J(\omega_H)\rangle$ values are comparable to those of backbone NH vectors in the flexible 50−59 segment, but $J(\omega_N)$ values are significantly smaller. This indicates that the density of frequencies of motions in the nanosecond time scale is lower but that the density of motions at frequencies around $\omega_H + \omega_N$ (i.e., 540 MHz) is about the same as for the NH in the unfolded segment. This suggests that side chains undergo complex motions at time scales different from those of the NH bonds of the 50−59 segment. The comparison of the spectral densities of these five arginine side chains shows that R29 and R57 exhibit significantly different behavior than the three others, R8, R14, and R43. They have large negative heteronuclear nOes and much smaller $J(0)$ and $J(\omega_N)$ values. This is easily understood for the side chain of R57, whose intrinsic fast dynamics is combined with the already fast dynamics of the backbone

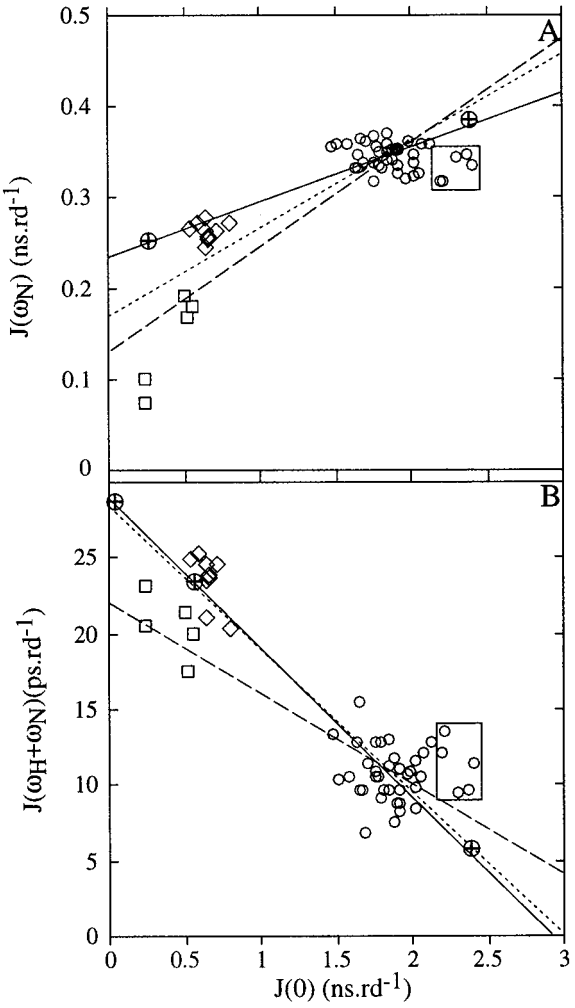

FIGURE 3: Plots of $J(\omega_N)$ (A) and $J(\omega_H + \omega_N)$ (B) as a function of $J(0)$. NH bonds of the backbone of the core are represented as open circles, NH bonds of the backbone of the 50−59 segment as open diamonds, and NH$^{\epsilon}$ bonds of arginines as open squares. The fits for set A (solid line), set B (dotted line), and set C (dashed line) as described in the text were obtained by linear regression. The five residues with high $J(0)$ that have been excluded for the fits are framed (i.e., V12, Y28, M39, R43, and H45). The circled plus symbols represent the points corresponding to the meaningful solutions of eqs 15 for set A.

in this region. The case of R29 is more interesting, since no special behavior of its NH vector backbone can be evidenced. It means that its side chain itself must have an independent, almost unconstrained mobility. This can indeed be understood through the analysis of the structure: the side chain of R29 is completely exposed to the solvent and is not stabilized by any ionic bridge. On the contrary, the side chains of R8, R14, and R43 are involved in ionic bridges with side chains of acidic residues: D4 for R8 and R14, E44 for R43. This is in agreement with the fact that the exchange rate of R29 Hϵ with water is much higher than those of the three others (unpublished results).

Analysis of the Correlations between $J(\omega_N)$, $\langle J(\omega_H)\rangle$, and $J(0)$. Figure 3 shows experimental values of $J(\omega_N)$ and $\langle J(\omega_H)\rangle$ plotted against the corresponding values of $J(0)$ for each available ^{15}NH bond. Three different groups can be distinguished: NH bonds of the backbone of the core (○), NH bonds of the backbone of the unfolded 50−59 segment (◇), and NH bonds of the arginine side chains (□). Three different data sets were thus analyzed separately and their

Table 1: Linear Regression Parameters in the Correlation between $J(\omega_N)$ and $J(0)$ and between $J(\omega_H + \omega_N)$ and $J(0)$ for the Three Data Sets A, B, and C[a]

set	linear equation	$\alpha_{(N/H)}^{(A/B/C)}$	$\delta\alpha_{(N/H)}^{(A/B/C)}$	$\beta_{(N/H)}^{(A/B/C)}$ (ns·rad^{-1})	$\delta\beta_{(N/H)}^{(A/B/C)}$ (ns·rad^{-1})
A	$J(\omega_N) = \alpha_N^A J(0) + \beta_N^A$	0.06	0.01	0.23	0.02
B	$J(\omega_N) = \alpha_N^B J(0) + \beta_N^B$	0.096	0.007	0.17	0.01
C	$J(\omega_N) = \alpha_N^C J(0) + \beta_N^C$	0.116	0.013	0.13	0.02
A	$\langle J(\omega_H)\rangle = \alpha_H^A J(0) + \beta_H^A$	−0.0099	0.0007	0.029	0.001
B	$\langle J(\omega_H)\rangle = \alpha_H^B J(0) + \beta_H^B$	−0.0095	0.0008	0.028	0.001
C	$\langle J(\omega_H)\rangle = \alpha_H^C J(0) + \beta_H^C$	−0.006	0.001	0.022	0.002

[a] Set A, NH bonds of the backbone; set B, all NH bonds (NH + NHϵ); set C, NH bonds of the core, including NHϵ.

Table 2: Values of the Correlation Times Obtained Using the Linear Correlation Approach[a]

set	$\tau_{N1}^{(A/B/C)}$ (ns·rad^{-1})	$\tau_{N2}^{(A/B/C)}$ (ns·rad^{-1})	$\tau_{H1}^{(A/B/C)}$ (ns·rad^{-1})	$\tau_{H2}^{(A/B/C)}$ (ns·rad^{-1})	$\tau_{H3}^{(A/B/C)}$ (ns·rad^{-1})
A	6.0 ± 0.2	0.67 ± 0.05	5.9 ± 0.2	1.42 ± 0.07	0.077 ± 0.003
B	5.8 ± 0.1	0.49 ± 0.03	6.0 ± 0.2	1.46 ± 0.09	0.075 ± 0.004
C	5.7 ± 0.1	0.38 ± 0.06	6.9 ± 0.7	1.98 ± 0.21	0.056 ± 0.006

[a] Values of the correlation times obtained from resolution of eq 23a,b for the three sets A, B, and C as described in the text. For τ_{N_i}, $i = \{1, 2\}$, values come from the linear correlation between $J(\omega_N)$ and $J(0)$. For τ_{H_i}, $i = \{1, 2, 3\}$, values come from the linear correlation between $J(\omega_H + \omega_N)$ and $J(0)$.

correlation lines are represented in Figure 3 [note that V12, Y28, M39, R43, and H45 with high $J(0)$ have been excluded for the calculation of the parameters since they would have biased the results]. In the first set (set A), only the NH vectors of the backbone were considered (solid lines). The second set (set B) included all the NH vectors for which data could be collected (dotted line). Finally, the third set (set C) contained all the NH vectors of the backbone and arginine side chains of the core of the protein (residues 1−45, dashed line). The mean values and standard deviations of linear correlations are given in Table 1. The linear correlations are quite good for the three sets, with regression factors around 0.9. The discrepancies between the parameters obtained for each set can be explained by the distinct dynamic behavior of NH vectors of the backbone of the core, NH vectors of the backbone of the 50−59 segment, and NH vectors of the arginine side chains. To go further into the interpretation of these results, an analytical expression of the spectral density is required (see Materials and Methods). The combination of eqs 6−8 leads to (*7*)

$$\forall k, \begin{cases} J_k(\omega_N) = \alpha_N J_k(0) + \beta_N \\ J_k(\omega_N + \omega_H) = \alpha_H J_k(0) + \beta_H \end{cases} \qquad (14)$$

The existence of a linear correlation indicates that the components $J_k(\omega)$ are the same for all residues. Each component $J_k(\omega)$ is related to specific motions that can be defined by a time scale. The dynamics of each NH bond is differentiated through the different weights of each motion, i.e., the different a_ks in eq 8. These differences are brought to light through the position of the experimental points, $\{J(0), J(\omega_N)\}$ or $\{J(0), J(\omega_H + \omega_N)\}$, along the correlation lines. To get a better idea about the number of contributions that should be taken into account, and their corresponding time scales, analytical expressions have to be used for each $J_k(\omega)$. These expressions can then be inserted in eq 14. If the models are correct, the corresponding correlation times and other possible motion parameters obtained from these two equations should be the same. In a first approach, the simpler case of brownian motions is considered. The combination of eqs 10 and 14 leads to two third-degree equations in τ:

$$\begin{cases} 2\alpha_N\omega_N^2\,\tau_N^3 + 5\beta_N\omega_N^2\,\tau_N^2 + 2(\alpha_N - 1)\tau + 5\beta_N = 0 & (15a) \\ 2\alpha_H(\omega_H + \omega_N)^2\tau_H^3 + 5\beta_H(\omega_H + \omega_N)^2\tau_H^2 + 2(\alpha_H - 1)\tau + 5\beta_H = 0 & (15b) \end{cases}$$

The roots of these equations are correlation times connected to the various motions contributing to the low-frequency (eq 15a) and high-frequency (eq 15b) part of the spectral density function. Using the distribution of $\alpha_{(N,H)}^{(A,B,C)}$ and $\beta_{(N,H)}^{(A,B,C)}$ obtained, the resolution of eqs 15 leads for each set (A, B, C) to six distributions of values of correlation times, $\tau_{N1}^{(A,B,C)}$, $\tau_{N2}^{(A,B,C)}$, $\tau_{N3}^{(A,B,C)}$, $\tau_{H1}^{(A,B,C)}$, $\tau_{H2}^{(A,B,C)}$, and $\tau_{H3}^{(A,B,C)}$. The first three ones come from the linear correlation between $J(\omega_N)$ and $J(0)$ and the last three ones come from the linear correlation between $\langle J(\omega_H)\rangle$ and $J(0)$. $\tau_{N3}^{(A,B,C)}$ is always negative and is not considered since it cannot have any physical meaning. Mean values and standard deviations are given in Table 2. On the basis of their magnitudes, $\tau_{N1}^{(A,B,C)}$ and $\tau_{H1}^{(A,B,C)}$ can be interpreted as global correlation times for the overall tumbling of the protein. The three other times, $\tau_{N2}^{(A,B,C)}$, $\tau_{H2}^{(A,B,C)}$, and $\tau_{H3}^{(A,B,C)}$, are shorter and should be related to internal motions. For $\tau_{N1}^{(A,B,C)}$ and $\tau_{H1}^{(A,B,C)}$, we considered the hypothesis of isotropic brownian motion as valid. As stated before, if all the NH bonds experience the same isotropic brownian motion at this time scale, the two distributions $\tau_{N1}^{(A,B,C)}$ and $\tau_{H1}^{(A,B,C)}$ should be compatible. This condition is better fulfilled for set A for which the side chains were not considered. The slightly poorer compatibility of τ_{N1}^{B} and τ_{H1}^{B} as compared to set A can easily be explained by the influence of the side-chain data. When only the NH bonds of the core are considered (backbone NH and NHϵ, set C), the two distributions do not overlap. The discrepancy between τ_{N1}^{C} and τ_{H1}^{C} indicates that motions of the side-chain vectors cannot be simply related to the dynamics of the backbone. Moreover, the largely dominant contribution of high-frequency internal motions to the spectral densities for these

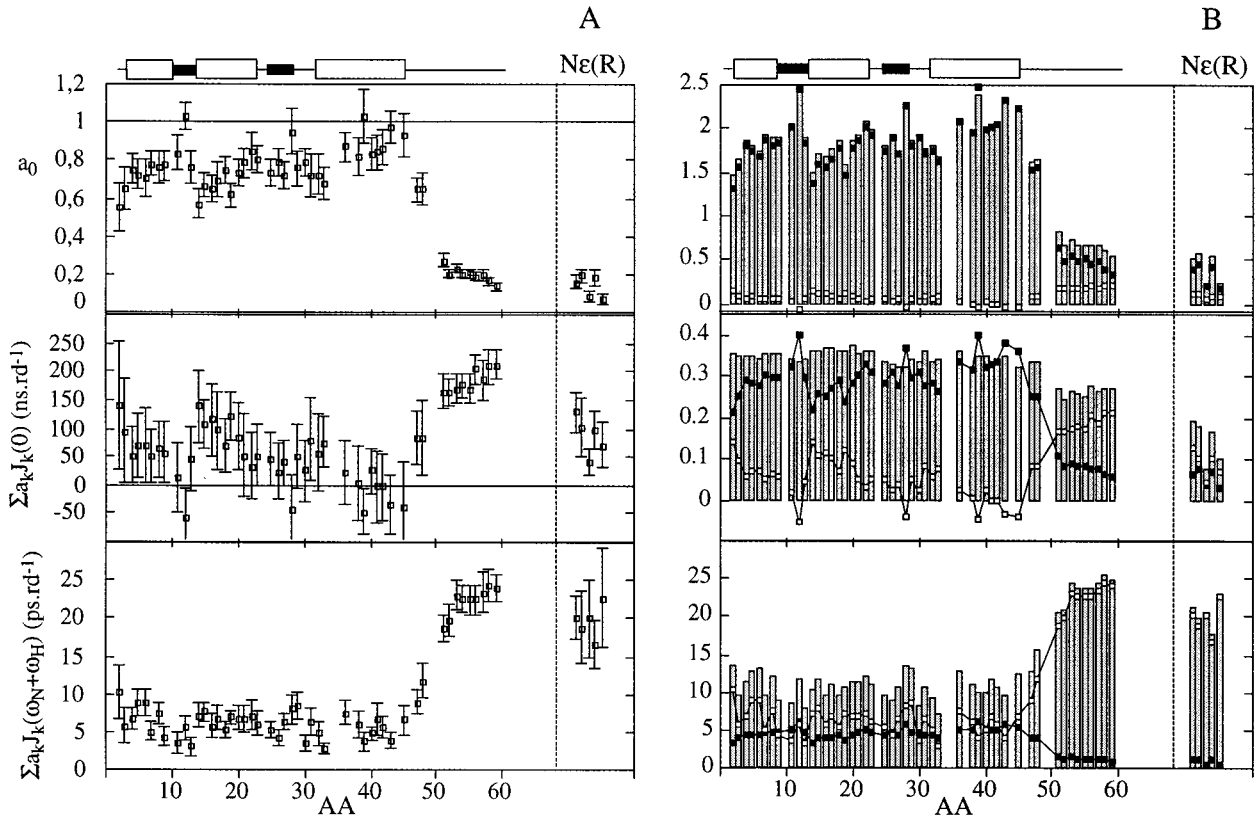

FIGURE 4: (A) Plots of the internal motion parameters obtained from eq 24 versus the protein sequence. From top to bottom: a_0, $\sum_{k=1}^{M} a_k J_k(0)$ in nanoseconds/radian, and $\sum_{k=1}^{M} a_k J_k(\omega_H + \omega_N)$ in picoseconds/radian. An overall tumbling correlation time of 5.95 ns·rad^{-1} was used for the calculation. (B) Distribution of the energy used for the overall tumbling [$a_0 J_0(\omega)$] (■) and for the internal motion [$\sum_{k=1}^{M} a_k J_k(\omega)$] (□) for the three available frequencies: top, $\omega = 0$; middle, $\omega = \omega_N$; and bottom, $\omega = \omega_H + \omega_N$. In the three cases, experimental spectral densities, which correspond to the sum of the two contributions, are represented as gray bars.

side-chain vectors could mask the contribution of the slower global correlation time and thus perturb the reliability of the results. We thus restricted the analysis to data set A of the backbone NH vectors.

Considering set A, it appears that coherent coupled motions of the NH vectors along the whole backbone of the protein exist with a correlation time equal to 5.95 ± 0.1 ns·rad^{-1} compatible with both distributions of τ_{N1} and τ_{H1}. This correlation time can be sensibly considered as the global correlation time of the protein. From eq 8, a system of three equations is obtained for the three spectral densities that allows the evaluation of the contribution of global and internal motions:

$$J(0) = a_0 J_0(0) + \sum_{k=1}^{M} a_k J_k(0)$$

$$J(\omega_N) = a_0 J_0(\omega_N) + \sum_{k=1}^{M} a_k J_k(\omega_N) \qquad (16)$$

$$J(\omega_N + \omega_H) = a_0 J_0(\omega_N + \omega_H) + \sum_{k=1}^{M} a_k J_k(\omega_N + \omega_H)$$

As the second term of the spectral density function is supposed to concern internal fast motions, it can be considered to be very flat from zero to ω_N. It is thus reasonable to equalize $\sum_{k=1}^{M} a_k J_k(0)$ and $\sum_{k=1}^{M} a_k J_k(\omega_N)$. The three unknown a_0, $\sum_{k=1}^{M} a_k J_k(0)$, and $\sum_{k=1}^{M} a_k J_k(\omega_N + \omega_H)$, can then be evaluated for each NH vector of the backbone from the three experimental spectral densities. A Lorentzian form was used for $J_0(0)$ with a τ_c equal to 5.95 ± 0.1 ns·rad^{-1} as determined above. The results are shown in Figure 4. In the core of the protein (residues 3−46, the five residues V12, Y28, M39, R43, and H45 being excluded), the mean values for a_0, $\sum_{k=1}^{M} a_k J_k(0)$, and $\sum_{k=1}^{M} a_k J_k(\omega_H + \omega_N)$ are respectively 0.75 ± 0.08, 57 ± 35 ps·rad^{-1}, and 6.0 ± 1.6 ps·rad^{-1}. In the 50−59 segment, mean values given in the same order are 0.20 ± 0.04, 184 ± 20 ps·rad^{-1}, and 22 ± 2 ps·rad^{-1}. Figure 4B highlights for each frequency (0, ω_N, and $\omega_H + \omega_N$) the weight of the two contributions, $a_0 J_0(\omega)$ and $\sum_{k=1}^{M} a_k J_k(\omega)$, associated with the overall tumbling and the internal motions, respectively. As expected from the experimental spectral densities, smaller values of a_0 in the 50−59 segment concur with higher values of $\sum_{k=1}^{M} a_k J_k(0)$ and $\sum_{k=1}^{M} a_k J_k(\omega_H + \omega_N)$. In this part of the protein, the contribution of high-frequency motions to $J(\omega_N)$ and $J(\omega_H + \omega_N)$ is higher than that of the overall tumbling. Upon looking more carefully to the core of the protein, slightly but significantly different behavior can be noticed for each secondary structure. NH backbone vectors of the turn and of the third helix have globally higher a_0 than the mean, associated with lower $\sum_{k=1}^{M} a_k J_k(0)$. However, their $\sum_{k=1}^{M} a_k J_k(\omega_H + \omega_N)$ are not significantly lower than the others. In particular, residue V12 in the turn and residues M39, R43, and H45 in the third helix give rise to negative, unphysical, $\sum_{k=1}^{M} a_k J_k(0)$ components. As stated

before, this is in favor of the hypothesis that, for these residues (and more generally in the turn and the third helix), there must exist some slow processes in the micro- to millisecond range. In this case, the assumption that $\sum_{k=1}^{M} a_k J_k(0)$ and $\sum_{k=1}^{M} a_k J_k(\omega)$ are equal is not achieved and yields erroneous values for $\sum_{k=1}^{M} a_k J_k(0)$. The NH bond of tyrosine 28, located in the turn between the second and the third helix, shows the same behavior. In the structure, the aromatic rings of Y28 and Y19 are tightly packed and maintain the loop and the second helix close together (*14*). Small displacements of the rings could then give rise to large chemical shift variations, leading to an efficient adiabatic relaxation pathway and an increase of the spectral density $J(0)$. Besides the global correlation time, three other correlation times, τ_{N2}^{B}, τ_{H2}^{B}, and τ_{H3}^{B}, were obtained from eqs 15 for set A. The first one, around 0.7 ns·rad^{-1}, comes from the linear correlation between $J(\omega_N)$ and $J(0)$; the two others, around 1.4 ns·rad^{-1} and 77 ps·rad^{-1}, come from the linear correlation between $J(\omega_H + \omega_N)$ and $J(0)$. The points $\{J(0), J(\omega_N)\}$ associated with τ_{N1}^{B} and τ_{N2}^{B} and the points $\{J(0), J(\omega_H + \omega_N)\}$ associated with τ_{H1}^{B}, τ_{H2}^{B}, and τ_{H3}^{B} are represented in Figure 3 by the circled marks on the solid lines related to set A. They represent the case of a single isotropic motion at the corresponding correlation time. It can be noticed that each experimental point of set A can indeed be described as a linear combination of Lorentzian functions. However, the two times τ_{N2}^{B} and τ_{H2}^{B} in the nanosecond range obtained from eqs 15 are comparable but not identical. This indicates the existence of complex internal motion in this time scale that cannot be strictly represented by a single Lorentzian. The fact that the faster correlation time does not appear from the correlation between $J(\omega_N)$ and $J(0)$ can be explained by the very small contribution of such fast motions to the value of $J(\omega_N)$.

Lipari and Szabo Parameters. The results of the fit of the three parameters (τ_c, S^2, τ_e) to the experimental spectral densities [$J(0)$, $J(\omega_N)$, and $\langle J(\omega_H)\rangle$] using eq 11 are shown in Figure 5. The global correlation time evaluated independently for each NH vector fluctuates significantly along the sequence, around an average value of 3.4 ± 0.3 ns·rad^{-1} in the 50−59 segment and between 4.6 ns·rad^{-1} (K2) and 6.6 ns·rad^{-1} (V12) in the core with a mean value of 5.6 ± 0.5 ns·rad^{-1}. The usual procedure using the mean value of $J(0)/J(\omega_N)$ over the residues in the secondary structures (*28*) leads to a correlation time equal to 5.5 ± 0.2 ns·rad^{-1} in the core of the protein. The parameters S^2, τ_e, and J_{ex} obtained from the seven minimizations with seven different τ_c values taken between 3 and 5.5 ns·rad^{-1} are shown in Figure 6A. These results show that the different values of τ_c do not affect the relative variation of the parameters along the sequence. The highest τ_c leading to values compatible with the experimental data in the core of the protein is equal to 5.0 ns·rad^{-1}. This value, however, still gives significantly negative values of J_{ex} for the NH vectors of the 50−59 segment and of arginine side chains. It thus cannot be considered as a real global correlation time but rather as a correlation time for the backbone of the core of the protein. A shorter correlation time of 3.2 ns·rad^{-1} has to be considered to correctly represent the experimental data in the 50−59 segment of the protein (Figure 6B). The generalized order parameters obtained using an overall correlation time equal to 5.0

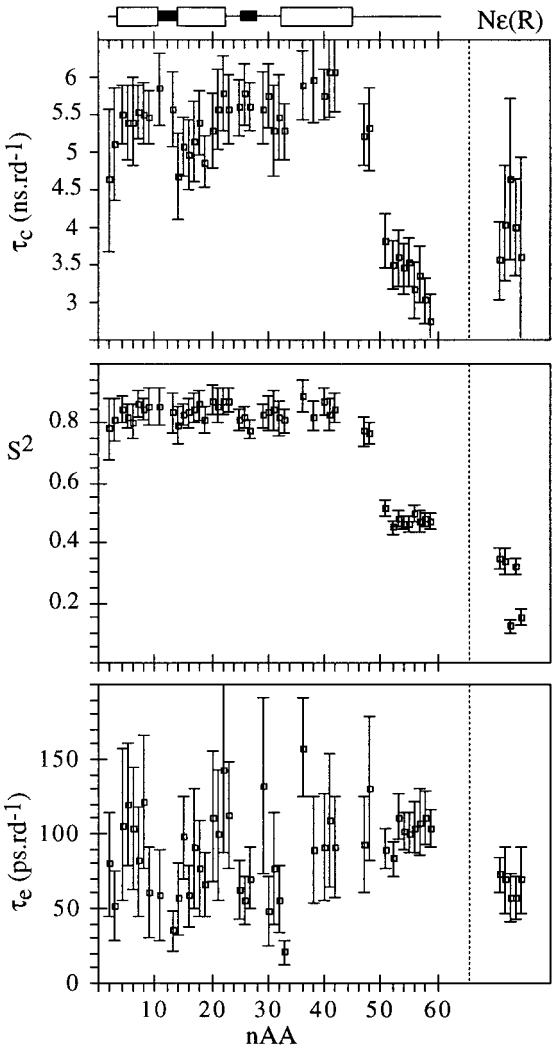

FIGURE 5: Plots of the relaxation parameters obtained using the Lipari and Szabo model with variable overall correlation times versus protein sequence. From top to bottom: overall correlation time τ_c in nanoseconds/radian, order parameter S^2, and internal fast-motion correlation time τ_e in picoseconds/radian.

ns·rad^{-1} in the core of the protein are in agreement with those generally found in globular proteins, with a S^2 going from 0.72 (Y28) to 0.84 (T16), and in average equal to 0.79 ± 0.03 over the core of the structure. Order parameters higher than 0.82 are all located in the second helix (T15, T16, A17, S18, V19, V20, and G23), order parameters lower than 0.76 in the core are all found in the second loop (K26, Q27, and Y28) and in the third helix (V38, V41, V42, and H45). Uncertainties on the two other parameters, J_{ex} and τ_e are quite high. Thus, no specific behavior can be outlined from the values of τ_e. However, for the exchange parameter, G11, V12, Y28, and most of the NH backbone vectors of the third helix (E36, V38, M39, V41, V42, R43, and H45) exhibit significantly higher values than the average value corresponding to an additional contribution to $R_N(N_{x,y})$ going from 3.5 to 6.5 s^{-1}. Finally, it should be underlined that the use of a global correlation time equal to 5 ns·rad^{-1} in the core of the protein does not allow us to obtain correct parameters compatible with the experimental data for the side chains of arginines 8, 14, 29, and 43 (see Figure 6A).

Equation 13 (extended Lipari and Szabo approach) was fitted to the experimental spectral densities using a global

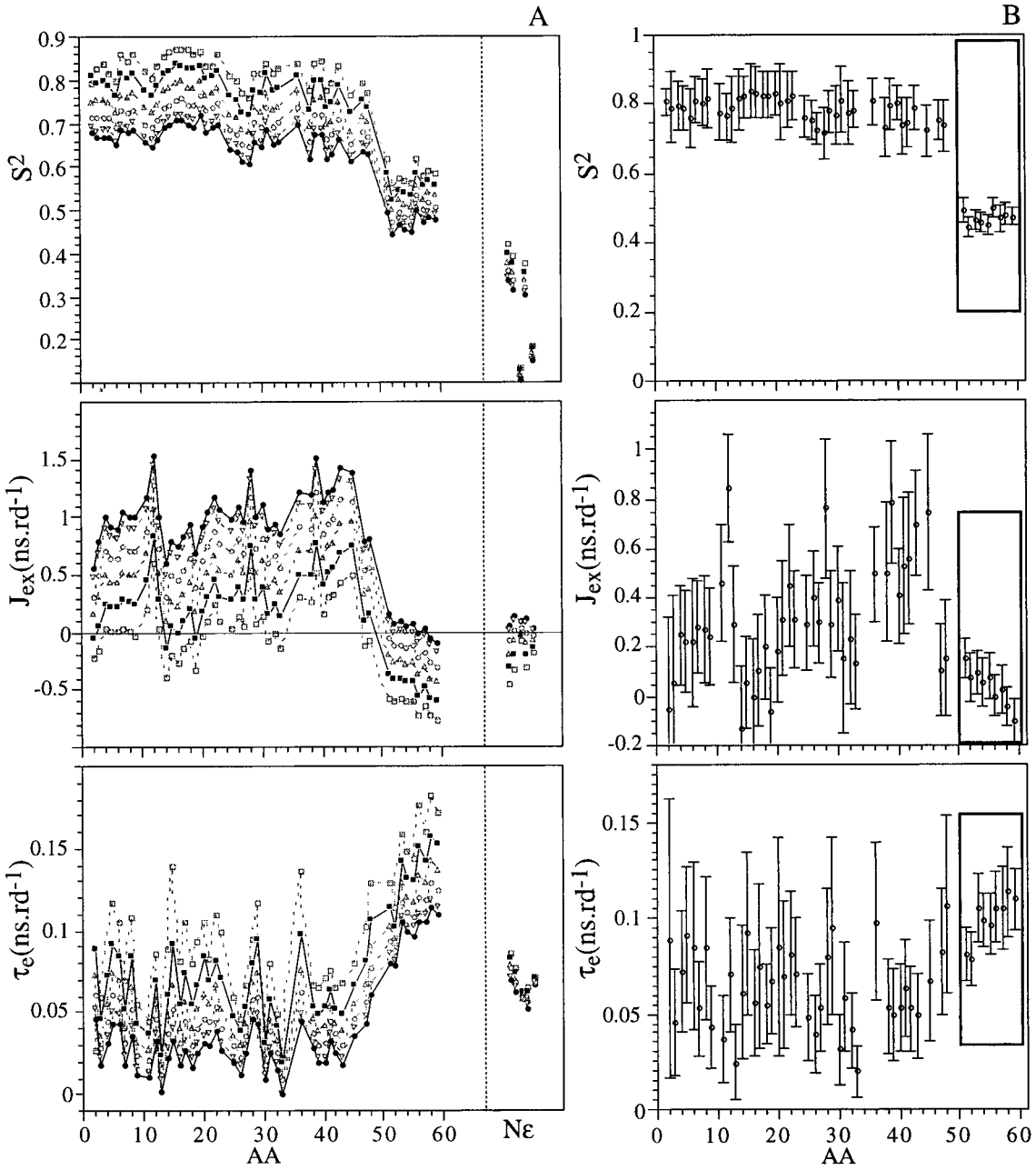

FIGURE 6: Summary of relaxation parameters fitting for FruR(1−57)* using the simple Lipari and Szabo model with a fixed overall correlation time τ_c. From top to bottom: order parameter S^2, supplementary contribution J_{ex} to $J(0)$ (eq 12) in nanoseconds/radian and internal fast-motion correlation time τ_e in picoseconds/radian. (A) Evolution of these three parameters for different values of the overall correlation time τ_c: 5.5 ns·rad^{-1} (□), 5.0 ns·rad^{-1} (■), 4.5 ns·rad^{-1} (△), 4.0 ns·rad^{-1} (○), 3.5 ns·rad^{-1} (▽), and 3.2 ns·rad^{-1} (●). (B) Retained parameters with uncertainty bars. An overall correlation time equal to 5.0 ns·rad^{-1} was retained in the core of the protein (white region), whereas another one equal to 3.2 ns·rad^{-1} had to be considered in the 50−59 segment (framed region).

correlation time τ_c equal to 5.95 ns·rad^{-1}. The results are shown in Figure 7. The most interesting result is the large contribution of slow internal motions to S^2 in the 50−59 segment of the protein as compared to the faster motions. The loss of coherence of NH bond motions due to internal dynamics is thus here largely due to intermediate time-scale motions. On the contrary, S_f^2 is much lower for the arginine side chains, showing that the motions of NH bonds in the picosecond time scale are less spatially restricted in arginine side chains than in the 50−59 segment of FruR(1−57)*. It should be noted that the data obtained on the arginine side chains can be well reproduced by this model. The order parameters S^2 obtained here are not compatible with the ones obtained with the simple Lipari and Szabo approach (Figure 8). Moreover, the use of a global correlation time shorter than 5.5 ns·rad^{-1} yields unphysical values of S_f^2 higher than 1 (data not shown).

Comparison of the Lipari and Szabo Parameters with the "Linear" Parameters. S^2 obtained from the extended Lipari and Szabo approach are identical within experimental errors to the a_0 obtained from the linear correlation approach (Figure 8). This result is in favor of the existence of intermediate time-scale internal motions that cannot be revealed in the simple Lipari and Szabo approach. To go further in the comparison, we assumed that the spectral density of internal motions can be approximated to a pure

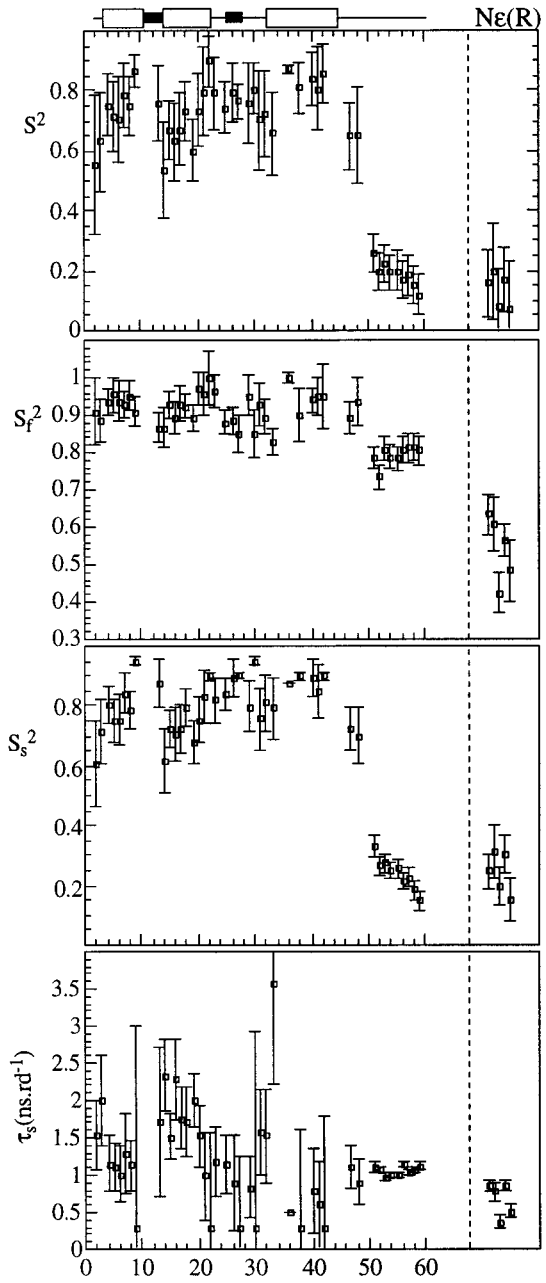

FIGURE 7: Plots versus the protein sequence of the relaxation parameters obtained using the extended Lipari and Szabo model with an overall correlation time τ_c equal to 5.95 ns·rad^{-1}. From top to bottom: generalized order parameter S^2, order parameter S_f^2 for fast internal motions, and order parameter S_s^2 for slow internal motions, and correlation time τ_s for slow internal motions in nanoseconds/radian.

Lorentzian. From eqs 8 and 10, one obtains

$$\sum_{k=1}^{M} a_k J_k(\omega_N) = \frac{2}{5}(1 - a_0)\frac{\tau}{1 + \omega_N^2\tau^2} \qquad (17a)$$

$$\sum_{k=1}^{M} a_k J_k(\omega_N + \omega_H) = \frac{2}{5}(1 - a_0)\frac{\tau}{1 + (\omega_N + \omega_H)^2\tau^2} \qquad (17b)$$

From these two equations, two possible internal correlation times, τ_N^+ and τ_N^-, are obtained from the value of $\sum_{k=1}^{M} a_k J_k(\omega_N)$, and two possible internal correlation times

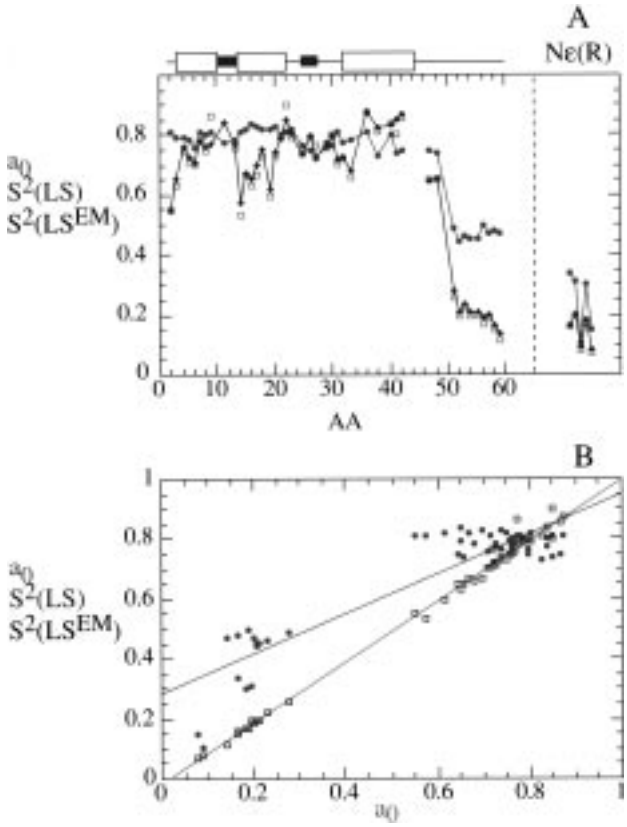

FIGURE 8: Comparison of the order parameters a_0 and S^2 obtained using the various approaches described in the text. (A) Plots versus protein sequence: linear correlation approach (red squares), simple Lipari and Szabo approach (green circles), and extended Lipari and Szabo approach (black diamonds). (B) Correlation plots as a function of a_0: simple Lipari and Szabo approach (green circles and green line); extended Lipari and Szabo approach (black squares and red line). The fits were obtained by linear regression.

τ_H^+ and τ_H^- are obtained from the value of $\sum_{k=1}^{M} a_k J_k(\omega_H + \omega_N)$ for each residue. τ_N^+ values (not shown) are all greater than the global correlation time and cannot be considered as internal correlation times. It can be noted that τ_N^-, τ_H^+, and τ_H^- are directly related to the internal correlation times τ_{N2}^B, τ_{H2}^B, and τ_{H3}^B, respectively, extracted from eq 15. However, τ_{N2}^B, τ_{H2}^B, and τ_{H3}^B correspond to internal correlation times for the whole set of NH bonds of the backbone and can be considered as some kind of average values; here, τ_N^-, τ_H^+, and τ_H^- are calculated independently for each residue. Comparisons of τ_N^-, τ_H^+, and τ_H^- with the internal effective correlation time τ_e and the slow internal correlation time τ_s are shown in Figure 9. Considering the rather high uncertainties for these parameters, we can conclude that, on one hand, τ_H^- and τ_e correlate quite well, and on another hand, τ_N^-, τ_H^+, and τ_s are comparable. In the case of the simple Lipari and Szabo model (eq 11), the second term in the analytical expression of the spectral density function at the two frequencies ω_N and $\omega_H + \omega_N$ corresponds to $\sum_{k=1}^{M} a_k J_k(\omega_N)$ and $\sum_{k=1}^{M} a_k J_k(\omega_H + \omega_N)$, respectively. Since τ_H^- and τ_e are comparable, it appears that the simple Lipari and Szabo approach leads us to select the fastest internal correlation time τ_H^- between the two possibilities τ_H^- and τ_H^+. If slower internal movements are indeed present, the contribution of internal motions at frequency ω_N obtained using this smaller internal correlation time becomes largely

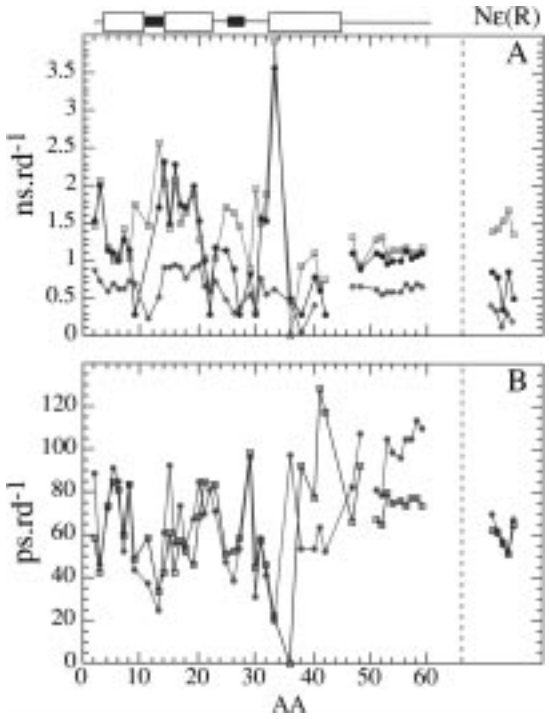

FIGURE 9: Comparison of internal correlation times obtained using the various approaches described in the text. (A) Slow internal correlation times, in nanoseconds/radian: τ_N^- (blue diamonds) and τ_H^+ (red squares) obtained from the linear correlation approach and τ_s obtained from the extended Lipari and Szabo approach (black circles). (B) Fast internal correlation times, in picoseconds/radian: τ_H^- (open squares) obtained from the linear correlation approach and τ_e obtained from the simple Lipari and Szabo approach (green circles).

underestimated. This effect is compensated by an overestimation of the order parameter S^2 and an underestimation of the global correlation time, thus allowing a good fit of the experimental data. This phenomenon appears clearly in Figure 7. The highest discrepancies between the S^2 values obtained from the simple Lipari and Szabo approach and the S^2 or a_0 obtained from the two other approaches are located in the second helix and in the 50−59 segment of the protein. The corresponding residues indeed have either higher τ_s in the case of the second helix or lower S_s^2 in the case of the 50−59 segment, indicative of a high proportion of internal motions in the nanosecond time scale. The global correlation times obtained correspond to an average between the real global correlation time and the slower time-scale internal motions. This explains the necessity of considering two different correlation times for the core and the C-terminal segment. In the case of the extended form of the Lipari and Szabo model, the slower internal correlation time τ_H^+ is selected. In this model, however, due to the influence of the faster internal motion taken into account through the S_f^2 factor (eq 13b), the second term of the spectral density at the frequencies ω_N and $\omega_H + \omega_N$ is not supposed to be exactly equal to $\sum_{k=1}^{M} a_k J_k(\omega_N)$ and $\sum_{k=1}^{M} a_k J_k(\omega_H + \omega_N)$. Moreover, the fact that τ_H^+ and τ_N^- are not equal shows that the spectral density for internal motions in the nanosecond time scale cannot be described by a unique Lorentzian function. Nevertheless, the order parameters S^2 obtained with this model stay compatible with the a_0 values. The good results obtained for the fits of (S^2, S_f^2, τ_s) seems thus due to a balance between S_f^2 and τ_s rather than a compensation of S^2 as was the case for the simple Lipari and Szabo model. This can be explained by the indeed small contribution of very fast motions to $J(\omega_N)$. The effective internal correlation time τ_s can then be considered as some kind of average value over the different types of internal motions.

It should be kept in mind that, since the time scale of the slower internal motions is the same as the time scale of the overall tumbling, these motions cannot be strictly considered as uncorrelated and the analytical expressions of the spectral density functions are not rigorously correct. No precise, quantitative conclusions should thus be drawn. However, the evaluation of a correlation time compatible with the three spectral densities $J(0)$, $J(\omega_N)$, and $J(\omega_H + \omega_N)$ from the linear correlation between them is strongly in favor of a concerted motion of all the backbone NH bonds consistent with a global correlation time equal to 5.95 ns·rad^{-1}.

Correlation between the Results of the Dynamics and the 3D Structure of FruR(1−57).* FruR(1−57)* appears to be divided into two dynamic regions. The first one comprises the globular subdomain and extends from residues 3 to 48. In this subdomain, internal motions are very restricted and are responsible for 25% on average of the decay of the correlation function. This decay occurs in two phases, a first very rapid one on the picosecond time scale and the second one on the nanosecond time scale. The NH bonds of the residues in the second helix show a slightly higher proportion of nanosecond time-scale motions. This helix being the DNA recognition helix, speculations can be made about the implication of such motions in DNA interaction. Residues in the turns and in the third helix appear to experience additional slow exchange processes. The role of these motions does not clearly appear. As no difference in the relative orientation of secondary structures was observed between the free and bound forms of DBD in this protein family, these motions could allow a local reorientation of the residues implicated in the DNA binding. It can be noted that the third helix appears less well defined than helices I and II in the reconstructed structures of FruR(1−57)*. The dynamic behavior of the connecting segment between helices II and III is homogeneous with that observed in the rest of the globular domain. This confirms that this segment is highly structured in FruR (*14*). On the contrary, in LacI DBD, this loop is poorly defined and shows increased mobility when compared to the rest of the DBD (*30*) while it gains a stable conformation when bound to its DNA operator. This discrepancy was related to the specificity of LacI for only one known DNA operator, while FruR is able to recognize specifically several operator sites (*14*). Our results are in agreement with the assumption that the mobility of side chains is essential to ensure selective and specific DNA base recognition.

The second region is the C-terminal end of the protein (50−59 segment). Its dynamic is characterized by a very low order parameter, lower than 0.2, and by a high amount of intermediate time-scale internal motions. This is fully compatible with the fact that this segment is completely unfolded. The two regions are linked by proline 49, which that could play the role of a hinge. From the analysis of the spectral densities of arginine side chains, it appears that the predominant contribution of very fast motions for ϵNH bonds does not allow us to obtain reliable results from the analysis of linear correlations between $J(0)$, $J(\omega_N)$, and $J(\omega_H + \omega_N)$.

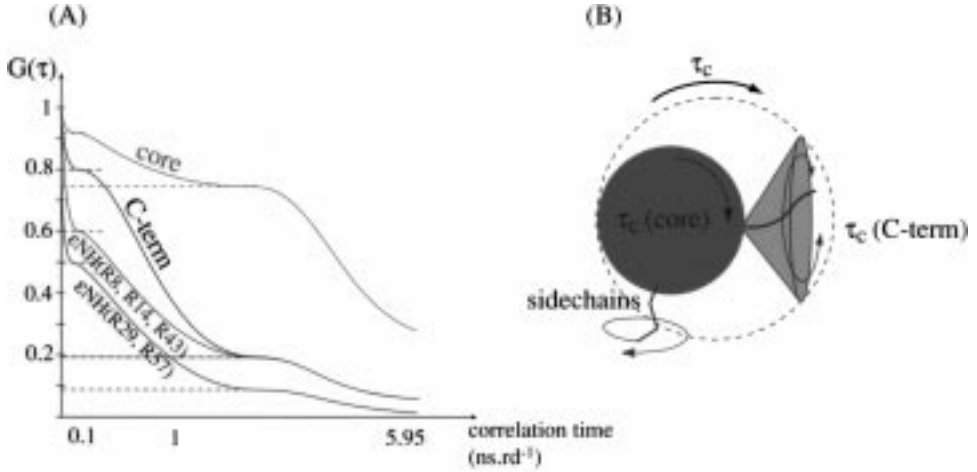

FIGURE 10: (A) Schematic representation of the autocorrelation functions of the NH bonds of the core (residues 3−46, red line), the NH bonds of the 50−59 segment (black line), the NHϵ bonds of R8, R14, and R43 (green line), and the NHϵ bonds of R29 and R57 (blue line) of FruR(1−57)*. These functions outline the different contributions of fast and intermediate time-scale internal motions along the protein. (B) Schematic representation of FruR(1−57)* illustrating the problem of the evaluation of a global correlation time when several segments in the protein have their own dynamic behavior.

Actually, it mainly shows that the dynamics of the side-chain bonds that are far from the backbone cannot be directly connected to the overall tumbling of the protein. However, a direct inspection of their spectral densities remains very informative. It shows that the ϵNH bond of arginine 29 is much more flexible on the picosecond time scale than the ϵNH bond of the three other arginines located in the globular subdomain. This is obviously related to the fact that the side chain of this arginine is completely exposed to the solvent and is not involved in a ionic bridge whereas the three others are. This also supports the suggestion that arginine 29 likely plays a major role in the specific recognition of FruR−DNA operators and FruR-DNA complex formation (*14*). Finally, most of the results obtained on the dynamics of FruR(1−57)* can be visualized on a schematic representation of the correlation functions for the different types of NH bonds of the protein (Figure 10).

CONCLUSIONS

We have shown here that a complete analysis of the spectral densities obtained from a reduced matrix approach allows us to gain insight into protein dynamics. Evidence for a concerted motion of all the NH bonds along the backbone with a correlation time equal to 5.95 ns·rad^{-1} was brought from the existence of a linear correlation between $J(0)$ and $J(\omega_N)$, and between $J(0)$ and $J(\omega_H + \omega_N)$. Further analysis of these correlations more generally showed that the spectral density function of each NH bond of the backbone can be described by using only a limited number of additional contributions associated with the same type of internal motion. The localization of the experimental points $\{J(0), J(\omega_N)\}$ and $\{J(0), J(\omega_H + \omega_N)\}$ along the correlation line is directly related to the distribution of the energy between the overall tumbling and the internal movements and is indicative of the degree of internal restraint of each NH bond motion. When compared to other usual models, the use of the extended Lipari and Szabo model for the spectral density function seems the most suitable in the case of FruR(1−57)* to evaluate more pictorial parameters about motions. The order parameters S^2 extracted from this model and the a_0 obtained without any assumption on the spectral density shape for the internal motions are compatible. This indicates that the spectral density function for internal motions can be nearly represented as the sum of two Lorentzian functions, one related to fast motions on the picosecond time scale and the other related to slower motions around 1 ns. On the contrary, the simple Lipari and Szabo expression for the spectral density function is not appropriate here and yields erroneous values for the global correlation time and the order parameter. The extensive analysis of the three spectral densities $J(0)$, $J(\omega_N)$, and $J(\omega_H + \omega_N)$ allowed the description of the dynamics of FruR(1−57)* over a large range of time scales, from picoseconds to milliseconds. This permitted us to precisely detail structural features of this DNA binding domain in the free state. The next step will be to analyze the evolution of the dynamics of the protein when bound to its operator, to understand better the role of the motions in the binding processes.

ACKNOWLEDGMENT

We thank J.-C. Cortay and D. Nègre for the overproduction of ^{15}N-labeled FruR and G. Deléage and C. Geourjon for their help in structure analysis.

SUPPORTING INFORMATION AVAILABLE

Table showing ^{15}N relaxation time constants and heteronuclear ^{1}H−^{15}N nOes at stationary state of FruR(1−57)* (2 pages). Ordering information is given on any current masthead page.

REFERENCES

1. Abragam, A. (1961) *The Principle of Nuclear Magnetism*, Chapter VIII, Clarendon Press, Oxford, England.
2. Peng, J. W., and Wagner, G. (1992) *J. Magn. Reson. 98*, 308−332.
3. Peng, J. W., and Wagner, G. (1992) *Biochemistry 31*, 8571−8586.
4. Markus, M. A., Dayie, K. T., Matsudaira, P., and Wagner, G. (1996) *Biochemistry 35*, 1722−1732.
5. van Heijenoort, C., Bouaziz, S. and Guittet, E. (1994) *J. Chim. Phys. 91*, 776−784.

6. Wagner, G. (1994) Approaches for Studies of Protein Mobility and Structure, The 35th Experimental NMR Conference, April 10−15, 1994, Asilomar, CA.
7. Lefèvre, J. F., Dayie, K. T., Peng, J. W., and Wagner, G. (1996) *Biochemistry 35*, 2674−2686.
8. Lipari, G., and Szabo, A. (1982) *J. Am. Chem. Soc. 104*, 4546−4559.
9. Lipari, G., and Szabo, A. (1982) *J. Am. Chem. Soc. 104*, 4559−4570.
10. Clore, G. M., Szabo, A., Bax, A., Kay, L. E., Driscoll, P. C., and Gronenborn, A. M. (1990) *J. Am. Chem. Soc. 112*, 4989−4991.
11. Clore, G. M., Kay, L. E., Driscoll, P. C., Wingfield, P. T., and Gronenborn, A. M. (1990) *Biochemistry 29*, 7387−7401.
12. Brennan, R. G. (1992) *Curr. Opin. Struct. Biol. 2*, 100−108.
13. Scarabel, M., Penin, F., Bonod, C., Nègre, D., Cozzone, A. J., and Cortay, J. C. (1995) *Gene 153*, 9−15.
14. Penin, F., Geourjon, C., Montserret, R., Böckmann, A., Lesage, A., Yang, Y. S., Bonnod-Bidaud, C., Cortay, J. C., Nègre, D., Cozzone, A. J., and Deléage, G. (1997) *J. Mol. Biol. 270*, 496−510.
15. Schumacher, M. A., Choi, K. Y., Zalkin, H., and Brennan, R. G. (1994) *Science 266*, 763−770.
16. Lewis, M., Chang, G., Horton, N. C., Kercher, M. A., Pace, H. C., Schumacher, M. A., Brennan, R. G., and Lu, P. (1996) *Science 271*, 1247−1354.
17. Spronk, C. A., Slijper, M., van Boom, J. H., Kaptein, R., and Boelens, R. (1996) *Nat. Struct. Biol. 3*, 916−919.
18. Kay, L. E., Nicholson, L. K., Delaglio, F., Bax, A., and Torchia, D. A. (1992) *J. Magn. Reson. 97*, 359−375.
19. Shaka, A. J., Baker, P. B., and Freeman, R. (1995) *J. Magn. Reson. 64*, 547−552.
20. Grzesiek, S., and Bax, A. (1993) *J. Am. Chem. Soc. 115*, 12593−12594.
21. Sklenar, V. J. (1995) *J. Magn. Reson. Ser. A 114*, 132−135.
22. Pons, J.-L., Malliavin, T. E., and Delsuc, M. A. (1996) *J. Biomol. NMR 8*, 445−452.
23. Skelton, N. J., Palmer, A. G., III, Akke, M., Kördel, J., Rance, M. and Chazin, W. J. (1992) *J. Magn. Reson., Ser. B 102*, 253−264.
24. Press, W. H., Flannery, B. P., Teukolsky, S. A., and Vetterling, W. T. (1988) *Numerical Recipes, in C— The Art of Scientific Computing*, Cambridge University Press, Cambridge, England.
25. Ishima, R. and Nagayama, K. (1995) *Biochemistry 34*, 3162−3171.
26. Farrow, N. A., Zhang, O., Szabo, A., Torchia, A., and Kay, L. E. (1995) *J. Biomol. NMR 6*, 153−162.
27. Brooks, C. L., III, Karplus, M., and Pettitt, B. M. (1987) *Proteins: A Theoretical Perspective of Dynamics, Stucture, and Thermodynamics*, pp 1−259, John Wiley and Sons, New York.
28. Kay, L. E., Torchia, D. A., and Bax, A. (1989) *Biochemistry 28*, 8972−8979.
29. Geourjon, C., and Deléage, G. (1995) *J. Mol. Graphics 13*, 209−212.
30. Slijper, M., Boelens, R., Davis, A. L., Konings, R. N. H., van der Marel, G. A., van Boom, J. H., and Kaptein, R. (1997) *Biochemistry 36*, 249−254.

BI971706H